

pubs.acs.org/JPCC Article

Gas Permeability and Selectivity of a Porous WS₂ Monolayer

Nasim Hassani, Mahdi Ghorbani-Asl, Boya Radha, Marija Drndić, Arkady V. Krasheninnikov, and Mehdi Neek-Amal*



Cite This: J. Phys. Chem. C 2021, 125, 25055-25066



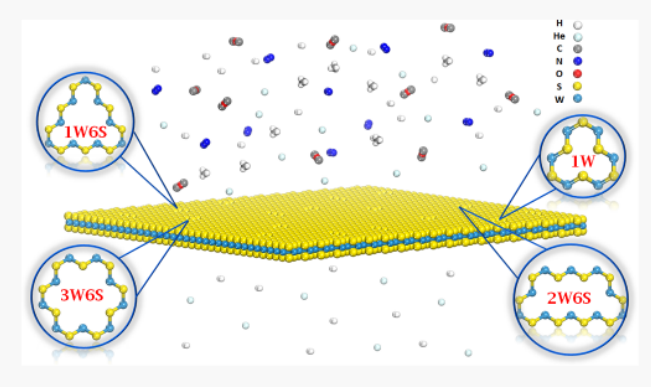
ACCESS

III Metrics & More

Article Recommendations

s Supporting Information

ABSTRACT: Atomically thin porous membranes display high selectivity for gas transport and separation. To create such systems, defect engineering of two-dimensional (2D) materials, e.g., via ion irradiation, provides an efficient route. Here, first-principles calculations are used to study the permeability of He, H₂, N₂, CO₂, and CH₄ molecules through WS₂ monolayers containing vacancy-type defects. We found that (i) for most pores, regardless of the pore size, H₂ exhibits large permeability ($\simeq 10^5$ GPU), (ii) dissociation of H₂ molecules and edge saturation occur when they approach the angstrom-size pores, (iii) the 1W6S pore (one W and six S atoms are removed from a WS₂ monolayer) can separate H₂ and N₂ gases with high selectivity, and (iv) the 2W6S pore exhibits exceptionally high selectivity for separation of H₂/CO₂ ($\simeq 10^{13}$)



and H_2/CH_4 ($\simeq 10^9$). Our study advances the understanding of the mechanisms behind gas permeability and selectivity through subnanometer pores in WS₂ and potentially other inorganic 2D materials.

■ INTRODUCTION

Membrane-based gas separation to isolate mixtures into pure phases of the gases is one of the most crucial steps in various chemical processes. Considering their atomically thin structures, two-dimensional (2D) materials are ideal candidates for the fabrication of ultrathin membranes with reduced transport resistance and high permeation. These applications, however, require construction of well-defined pores in 2D materials with radii of a few nanometers. Irradiation with energetic particles, such as ions or electrons, ultraviolet-based oxidative etching, and high-temperature self-organized growth reactions have been suggested for fabrication of porous 2D materials.

The existing porous 2D membranes have already shown ultrahigh flux and selectivity for gas mixture separation $^{7-11}$ and water desalination. 12,13 As a prominent example, permeance P of small molecules through porous graphene increases in the order $P(\mathrm{CO}_2)^{14-16} < P(\mathrm{CH}_4)^{14,15} < P(\mathrm{N}_2)^{14-18} < P(\mathrm{H}_2)^{17,18} < P(\mathrm{He})^{19}$ with pore sizes being within the range of 3.72–8.64 Å. For example, the permeance through a graphene pore with an effective diameter of 2.57 Å was found to be 2.8 \times 10 5 GPU for hydrogen molecules. 20,21

In another study, Sun et al.²² studied gas transport through porous graphene with one missed carbon atom ring having an effective diameter of 2 Å. It was found that helium and hydrogen can permeate through such a porous membrane, which is not the case for methane and xenon. Moreover, it was revealed that a high density of atomic-scale defects in graphene, where the graphene structure contains five-, six-,

seven-, and eight-carbon atom rings, can block molecular transport except protons and lithium ions.²³ They demonstrated that the energy barrier decreases on increasing the number of atoms in the rings. In addition, protons bind to the carbon atoms at the pore mouth when they permeate through the pores, which contain an eight-carbon atom ring.

Recently, porous WS₂ monolayers were revealed to be mechanically stable and to act as atomically thin barriers to helium transport.²⁴ The results indicated a fast helium flow ($\simeq 10^{-13}$ mol s⁻¹) through pores fabricated using a focused ion beam with sizes ranging from 1.05 up to 6.20 Å.²⁴ Efficient H₂/CO₂ separation with high H₂ permeability (1200 Barrer) was reported through a thick MoS₂ membrane.²⁵ In addition, numerous theoretical studies have been carried out to elucidate the transport mechanisms of gas permeation and selection through sub-nanometer graphene, hexagonal boron nitride, and MoS₂ ²⁷⁻²⁹ pores.

The gas flux through sub-nanometer pores in the simplest theoretical approach is described using the following approximations: (i) Knudsen mechanism for the direct gas impingement when the pore size is much larger than the molecular size but still smaller than the molecule mean free

Received: August 4, 2021 Revised: October 20, 2021 Published: November 9, 2021





path,³⁵ (ii) the empirically added Arrhenius factor is used to modify the permeance for considering the translocation energy barrier when the pore size is comparable to the size of the gas molecules,³⁶ and (iii) transition state theory (TST) for the translocation step associated with an energy barrier.^{7,8,37} Furthermore, the analytical potential molecular dynamics (MD) simulations are usually used to quantify permeance through nanopores.^{38–41} Such methods, however, require a careful choice of the simulation parameters and the results strongly depend on the accuracy of the employed force fields. So far, most of the reports on the permeability through porous 2D materials are focused on graphene,^{42–47} hexagonal boron nitride,⁴⁸ and MoS₂,^{27,52,53} while there is no systematic study on the permeance and selectivity of other transition metal dichalcogenides (TMDs) such as WS₂.

In addition to gas permeation and separation, porous 2D materials are also interesting in the context of catalysis and gas storage. The creation of nanopores can introduce reactive sites on the inert basal plane of the 2D membrane, which can be subsequently used for catalytic applications. The electrochemical activity of edge-dominated 2D membranes was employed for fuel generation, such as the hydrogen evolution reaction (HER) 30,32 or the oxygen evolution reaction (OER). For example, it was shown that sulfur vacancy in the basal plane of MoS $_2$ leads to hydrogen storage at room temperature. The dissociation and chemisorption of H $_2$ depends on the S-vacancies, resulting in the physisorption of incoming H $_2$ molecules.

Here, using density functional theory (DFT) calculations, we systemically investigate the permeability and selectivity of helium (He), hydrogen (H_2), nitrogen (N_2), carbon dioxide (CO_2), and methane (CH_4) gases for translocation through various pores with sub-nanometer sizes in the WS₂ monolayer. Using ab-initio MD simulations, we tested the stability of porous WS₂ to ensure the stable shape and size of the studied pores at room temperature, consistent with experiments. He further found that H_2 has a lower activation energy barrier among other gases (e.g., N_2 and CO_2). In addition, the results showed the dissociation of H_2 molecules during the translocation through some of the pores. The porous WS₂ monolayers exhibit high selectivity for separation of H_2/CO_2 and H_2/CH_4 motivating their applications in the field of gas filtration.

METHODS

First-Principles Calculations. The DMol³ module of the Materials Studio software was used to perform all DFT calculations.⁵⁴ The generalized gradient approximation (GGA) with Perdew-Burke-Ernzerhof (PBE) functional⁵⁵ was adopted in conjugation with the double numerical plus polarization (DNP) basis set.⁵⁶ The transition states (TSs) were searched by performing a linear synchronous transit (LST), followed by the repeated conjugate gradient (CG) minimizations.⁵⁷ Long-range vdW interactions were taken into account using the Tkatchenko-Scheffler van der Waals correction method.⁵⁸ The global orbital cutoff and the selfconsistent field (SCF) convergence threshold were set to 6.0 Å and 10^{-6} au, respectively. To avoid the interaction of two adjacent layers, a vacuum layer of 15 Å was introduced perpendicular to the basal plane. The full geometry optimization was performed until the atomic forces were less than 0.05 eV/Å. The optimized crystal lattice parameters of porous WS2 monolayers are tabulated in Table S1.

The Hirshfeld⁵⁹ charge analysis is employed to evaluate charge transfer between the porous WS₂ membrane and the molecules. This methodology quantitatively describes the charge distribution in the system by dividing into suitable atomic fragments. The usual approach is to share the charge density at each point between the atoms, commensurate with the density of isolated atoms at similar distances from the nuclei. This methodology provides a localized distribution of atoms that were bonded together and the molecular density monotonously spread in their vicinity. By integrating the density of bonded atoms minus the density of free atoms, the net atomic charges can be calculated. This calculation gives the charges transferred between molecules or between two different parts of the system.

Ab-Initio MD. Ab-initio molecular dynamic simulations were performed using the Vienna ab initio simulation package (VASP). The simulations are performed on a 22.11 Å × 22.11 Å supercell of monolayer WS $_2$ containing 147 atoms. A plane-wave energy cutoff of 300 eV was used, and the Brillouin zone was sampled with a 5 × 5 × 1 k-mesh grid. A microcanonical ensemble (NVE) was simulated, and the MD time steps were set to 1 fs.

For all types of pores, different possibilities of adsorption positions have been investigated and the most stable configurations were used for translocation energy barrier calculations. The incident molecule/atom was placed perpendicular to the WS₂ monolayer at a distance of 20 Å. The initial energies of the injected molecule/atom were set based on the calculated DFT results of the adsorption energy ($E_{\rm ads}$). The simulation setup designed to inject a typical atom/molecule onto the defected WS₂ monolayer is presented in Figure S7.

Translocation Energy Barrier. The energy barrier (Δ) for gas flow through a given pore can be calculated using ⁶¹

$$\Delta = (E_{\rm TS} - E_{\rm IS}) \tag{1}$$

where $E_{\rm TS}$ and $E_{\rm IS}$ are the total energy of the initial state (IS) and transition states (TSs), respectively. Notice that this is the barrier associated with direct impingement (perpendicular to the surface of the WS₂ monolayer). For surface diffusion, another barrier should be taken into account.

Kinetic Theory. Integrating the Maxwell distribution for the particle velocity over all appropriate velocities and above a plane located at z=0 containing the pore with area A gives the number of atomic or molecular collisions with a pore wall per unit area per unit time (the impingement rate). If the impingement rate is combined with ideal gas law ($\Pi V = Nk_{\rm B}T$), the effusion flow rate P (can be named permeance) is written as

$$P = \Pi / \sqrt{2\pi MRT} \tag{2}$$

where Π is the pressure difference between the feed side and the permeate side, M is the molar mass, $k_{\rm B}$ is the Boltzmann constant, R is the universal gas constant, and T is the gas temperature. Equation 2 is the effusion rate equation. An additional factor to eq 2, i.e., the sticking coefficient of gas molecules onto the surface, is given by $\alpha = A/A_0$ (the ratio of the cross-sectional area of the aperture and the area of the porous membrane A_0). If the pore diameter $(D_{\rm p})$ is comparable to the kinetic diameter $(k_{\rm d})$, the Arrhenius factor is empirically added to the permeance P, which originates from the gas—pore repulsive interaction

$$P = (\alpha \Pi / \sqrt{2\pi MRT}) e^{(-\Delta/k_B T)}$$
(3)

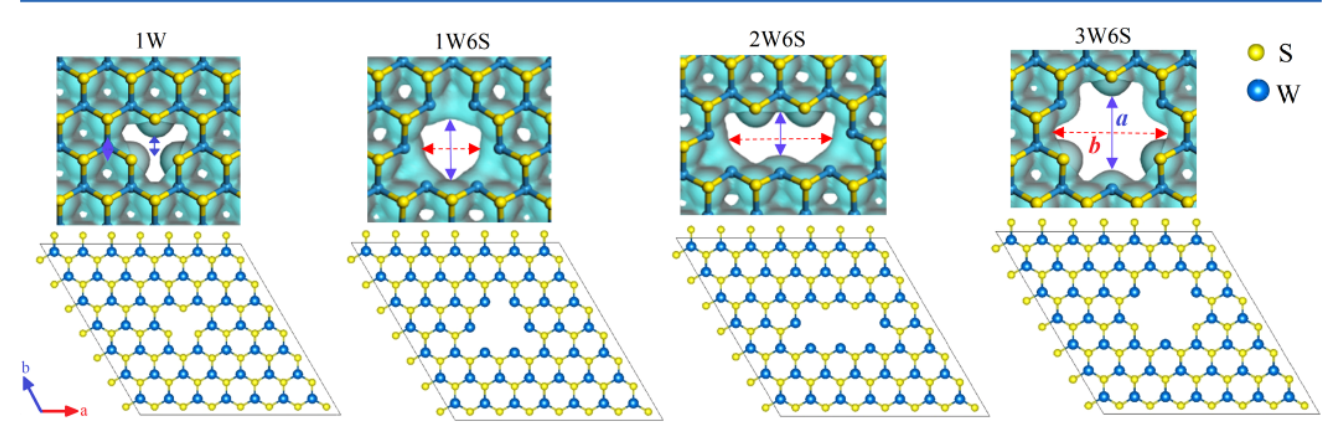


Figure 1. Atomic structures of the WS₂ monolayer with various vacancy-type defects, where the nomenclature used corresponds to the types and numbers of missing atoms. The supercells used in simulations are also shown, along with the electron density isosurfaces (isovalue of 0.2 e/Å³). a and b indicate the width and the length of the defect, respectively, as depicted in the images.

where Δ is the activation energy required for the translocation of particles through the pore. Since the Knudsen number (λ/L) for our porous membranes is much larger than 1 (the mean free path of an ideal gas $(\lambda \simeq 0.1 \text{ mm})$ is much larger than the gap length $(L \approx 0.5 \text{ nm})$, here, the distance between two S-layers of porous WS₂), one should consider the free molecular flow conditions as expressed by eq 2.

RESULTS AND DISCUSSION

Porous WS₂ Monolayer. The translocation of molecules across nanopores for different applications necessitates the deliberate creation of pores of varying sizes and shapes. We considered four types of defects, which were observed in recent experiments,²⁴ where the WS₂ monolayer was bombarded using gallium ions. The optimized structures of porous WS2 monolayers are shown in Figure 1. The details of firstprinciples calculations are presented in the Methods section. In addition to single W vacancy, defects with three missing sulfur and N missing tungsten atoms (N = 1, 2, 3), labeled as "NW6S" pores, are studied. However, the S vacancies and other complex point defects with small effective diameters would not impact the pore separation application even if they were made. Therefore, we studied the nanopores that are larger in size with pore diameters of $D_p = 1.05$, 3.15, 2.10, and 5.25 Å for 1W, 1W6S, 2W6S, and 3W6S pores, respectively (see Table 1), which were reported in recent experimental work.²⁴ Since these pores are not circular but have geometric shapes defined by the 2D lattice, for practical purposes, here, we defined the effective diameter D_p of the pores, as illustrated in Figure 1 (see also Table 1).

Table 1. (A) Size of Studied Pores, Width (a), Length (b), and Effective Diameter (D_p) , and (B) the Kinetic Diameter (k_d) of the Studied Gases

	(A	A)		(В)
defect	a (Å)	b (Å)	D _p (Å)	gas	k _d (Å)
1W	1.05	1.05	1.05	He	2.60
1W6S	3.15	3.15	3.15	H_2	2.89
2W6S	6.20	2.10	2.10	CO_2	3.30
3W6S	5.25	5.25	5.25	N_2	3.64
				CH_4	3.80

The formation of these defects under ion irradiation can be understood in the following way: the probability of S sputtering is much higher than that of W sputtering due to the lower displacement threshold energies for S atoms than for W atoms. ⁶² On the other hand, the impact of the ions into W atoms is likely followed by energy transfer from the recoil W atom to S atoms, eventually leading to the creation of pores. In addition, the presence of a substrate may also enhance defect production in supported 2D materials due to indirect sputtering caused by backscattered ions and atoms sputtered from the substrate. ^{10,63}

Molecular electrostatic potential (MEP) provides information on the interaction of gas molecules with the materials. 64 In the MEP map of porous WS $_2$ (see Figure S1), the positive MEP (blue color) is located inside the pore region, which imposes an attractive interaction between the pores and molecules with a high electron density. The electrostatic interactions affect the energy barrier for gas molecule passage through the nanopore.

For the studied molecules, the calculated isotropic polarizabilities are listed in Table S2, which are in agreement with previous reports. 65,66 In general, on increasing the size of the atom/molecule, the polarizability and induced dipole moment increase. Moreover, the larger polarizability enhances the interaction of molecules with the surface because of the rearrangement of induced charge on the surface.⁶⁷ The polarizability of the studied atom/molecules follows the order CO₂ > CH₄ > N₂ > H₂ > He. It is found that at a constant height above the pore, the adsorption energy and the activation energy barrier correlate with the polarizability and follow the same trend. Notice that evaluating the induced dipole moment of gases as they move into the pore may provide insights into the adsorption energy and activation barriers. The dipoles change with the size of pores and the type of approaching molecule, which consequently affects the mutual interaction between the pore and the particles. The effects of the dipoles correlate with the aforementioned charge redistribution, which is automatically included in the adsorption energy and activation energy calculations.

Using ab-initio molecular dynamics simulation at room temperature for a 5 ns time interval, we did not find any pore-shape deformation. Two typical snapshots of the optimized systems at room temperature are shown in Figure S2. This confirms that the pores are stable with negligible change in

Table 2. Optimized Parameters for Adsorption of He, $H_2(\perp \text{ and } \parallel)$, $2H_2$, $3H_2$, $N_2(\perp \text{ and } \parallel)$, CO_2 , and CH_4 over Porous WS₂ Monolayers, the Adsorption Energy (E_{ads}) , Vertical Distance from the WS₂ Monolayer (h_{ads}) , Inner Bond Length between Atoms of the Adsorbed Molecule (d), and the Charge Transferred from the WS₂ Monolayer to the Gas Molecule $(Q)^a$

membrane	gas molecule	$E_{\rm ads}$ (eV)		h_{ads} (Å)	d (Å)	() (e)
1W	He	-0.04		3.51			0.00
	$H_2(\perp)$	-0.15		2.88	0.75	-	-0.06
	$H_2(\parallel)$	-0.24		2.65	0.75	-	-0.02
	$N_2(\perp)$	-0.22		3.55	1.11		0.00
	$N_2(\parallel)$	-0.24		3.23	1.11		0.00
	CO_2	-0.08		3.30	1.16	-	-0.06
	CH ₄	-0.05		2.37	1.09		0.00
1W6S	He	-0.07		1.20			0.00
	$H_2(\perp)$	-0.25		0.00	0.75	-	-0.10
	$H_2(\parallel)$	-2.95		0.00	2.45	-	-0.46
	$2H_2$	-5.32		0.00		-	-0.73
	$3H_2$	-7.22		0.00		-	-1.11
	$N_2(\perp)$	-0.34		1.01	1.11	-	-0.03
	$N_2(\parallel)$	-0.20		1.83	1.11		0.00
	CO ₂	-0.11		3.21	1.16	-	-0.01
	CH ₄	-0.39		0.00	1.10	-	-0.10
2W6S	He	-0.05		2.08			0.00
	$H_2(\perp)$	-1.13		0.00	0.89	-	-0.14
	$H_2(\parallel)$	-1.24		0.00	0.88	-	-0.18
	$2H_2$	-3.69		0.00		-	-0.61
	$3H_2$	-6.04		0.00		-	-0.99
	$N_2(\perp)$	-0.30		2.07	1.11	-	-0.03
	$N_2(\parallel)$	-0.28		2.52	1.11		0.00
	CO_2	-0.34		0.00	1.16		-0.10
	CH ₄	-0.23		1.28	1.10	-	-0.07
3W6S	He	-0.06		0.00			0.00
	$H_2(\perp)$	-0.22		0.00	0.75		-0.11
	$H_2(\parallel)$	-0.23		0.00	0.86		-0.14
	$2H_2$	-1.77		0.00			-0.30
	$3H_2$	-4.16		0.00			-0.64
	$N_2(\perp)$	-0.26		0.00	1.11		-0.04
	$N_2(\parallel)$	-0.25		0.00	1.12		-0.03
	CO_2	-0.18		0.00	1.17		-0.08
	CH ₄	-0.21		0.00	1.10	-	-0.05
	pore size (Å)	He	H ₂ (⊥)	E _{ads}	N (1) N (II)	CO ₂	CH ₄
1 1 1 68	-			$H_2(\parallel)$	$N_2(\perp)$ $N_2(\parallel)$	CO_2	
graphitic carbon nitride ⁶⁸ 2D covalent triazine framework ⁶⁹	4.76	-0.02	-0.09		-0.13	0.15	-0.15
2D covalent triazine framework ³ porous graphene ⁷⁰		-0.03	-0.05	0.15	-0.12	-0.15	-0.19
porous graphene ⁷⁰	3.75	-0.03		-0.15	-0.23		-0.34 -0.19
porous graphene ⁷⁰	3.92	-0.03		-0.07	-0.14		
porous graphene fused pentagon network 71	5.50	-0.04		-0.07	-0.10	0.22	-0.21
	3.00	0.04		-0.20	-0.26	-0.22	-0.25
graphenylene ⁷²	5.34	-0.04			-0.13	-0.15	-0.17
graphenelike poly(triazine imide)	3.88				-0.17	-0.25	

^aThe bold numbers are those with lower adsorption energy. For comparison, the adsorption energy of gas molecules over other 2D materials is listed.

size, at least within this simulation time interval, which is in agreement with the experiment.²⁴

Adsorption Energy. To gain insights into the adsorption of gases on the porous WS_2 monolayer, we first evaluated the adsorption energy (E_{ads}) of a gas molecule as

$$E_{\rm ads} = E_{\rm system} - (E_{\rm total} + E_{\rm gas}) \tag{4}$$

where $E_{\rm system}$ is the total energy of the gas/porous WS₂ monolayer and $E_{\rm total}$ and $E_{\rm gas}$ are the energies of the bare porous WS₂ monolayer and of the gas molecule, respectively. The results of $E_{\rm ads}$ for these gases are tabulated in Table 2.

To study the adsorption of H_2 and N_2 molecules, two possible orientations of these molecules, perpendicular (\bot) or parallel (\parallel) with respect to the basal plane of WS $_2$, were considered. The lower energy values for these two orientations are boldfaced in Table 2. In the case of linear molecules (e.g., H_2 and N_2), the most stable adsorption location is when they are above the pore's center and the molecules are perpendicular to the WS $_2$ plane. The exceptions are the configurations of N_2 over 1W and 3W6S and H_2 over 1W6S. Whereas for CO $_2$ and CH $_4$ molecules, the perpendicular and one-hydrogen head orientations are the most likely orienta-

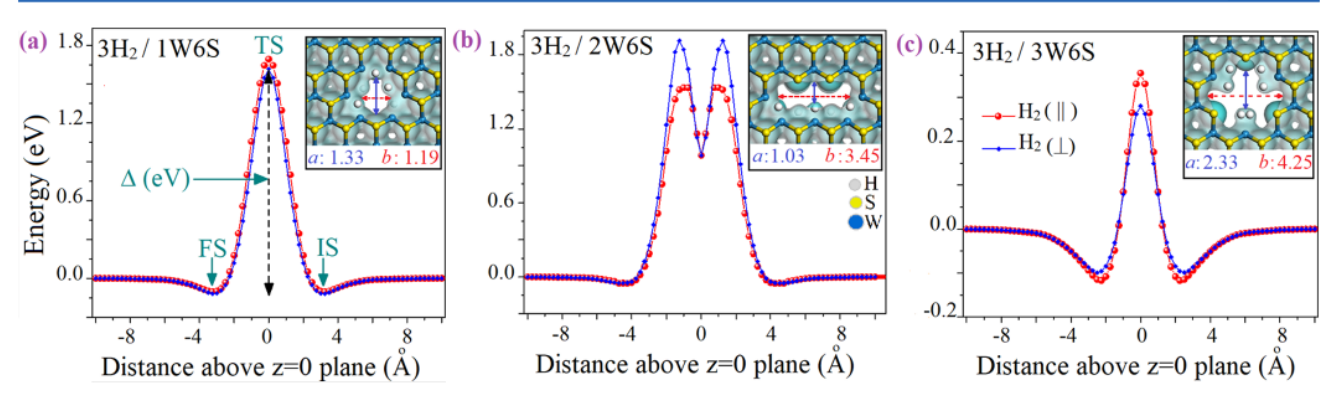


Figure 2. Energy profiles for H_2 passing through the aperture of porous WS_2 monolayer with hydrogenated 1W6S, 2W6S, and 3W6S. In (a) the position of the initial state (IS), transition state (TS), and final state (FS) on the interaction energy profile is demonstrated. The insets are the electron density isosurfaces corresponding to porous WS_2 monolayer with hydrogenated pores 1W6S (a), 2W6S (b), and 3W6S (c). The value of isovalue is 0.2 e/Å^3 .

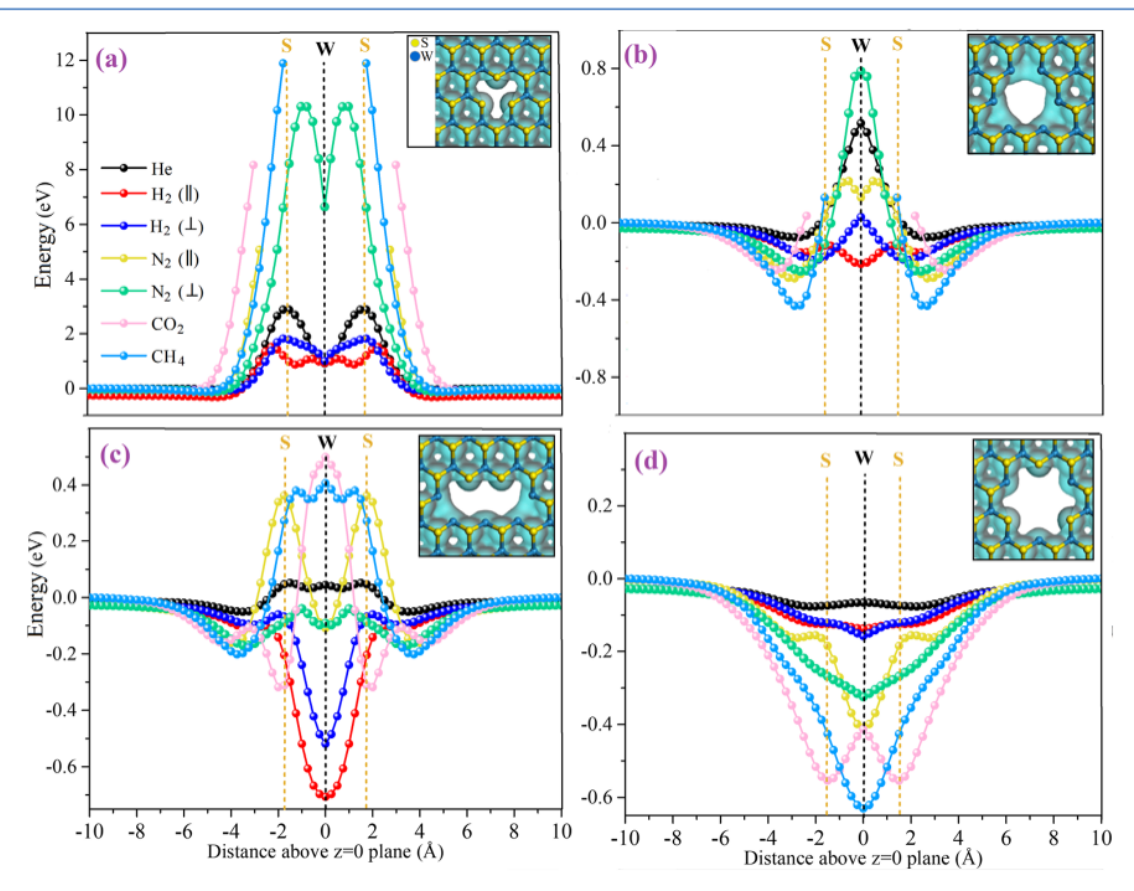


Figure 3. Interaction energy profiles for He, $H_2(\perp, \parallel)$, $N_2(\perp, \parallel)$, CO_2 , and CH_4 passing through the aperture of the porous WS₂ monolayers: (a) 1W, (b) 1W6S, (c) 2W6S, and (d) 3W6S. The insets show the corresponding electron density isosurfaces (isovalue of 0.2 e/Å³).

tions for approaching the WS₂ monolayers. The adsorption height, $h_{\rm ads}$ i.e., the vertical distance between gases and pores, is tabulated in Table 2. It should be mentioned that the considered molecules can be also adsorbed on the surface of the WS₂ monolayer that has been studied at length. Figure S3 indicates the most favorable sites for the adsorption of various gases such as He, H₂, N₂, CO₂, and CH₄. We found that (i) the adsorption heights for all of the studied molecules are larger than 2 Å and (ii) in most cases, the bond lengths (d) between atoms in the adsorbed molecules change only slightly (see Table 2). For comparison, the adsorption energies of the

molecules on other porous 2D materials, reported in the literature, are also presented in Table 2.

Hydrogen Molecule Dissociation and Pore Edge Atom Saturation. Due to the presence of undercoordinated atoms at the pore, the strong chemisorption of the $\rm H_2$ molecules with edge atoms is expected. This strong interaction between the absorbent and the pore leads to an increase in the bond length of the $\rm H_2$ molecule and eventually dissociation on the pore edge. In the case of adsorption on 1W6S pores, the bond length of the $\rm H_2$ molecule increased significantly from 0.75 to 2.45 Å, corresponding to an electron transfer of -0.46lel from the WS $_2$ to the $\rm H_2$ molecule.

Table 3. Calculated Energy Barrier (Δ, eV) for Different Gas Molecules through the Porous WS₂ Monolayers^a

membrane	pore size (Å)	He	$H_2(\perp)$	$H_2(\parallel)$	$N_2(\perp)$	$N_2(\parallel)$	CO_2	CH ₄
1W	1.02	2.91(3)	1.90(3)	1.82(4)	10.42(3)			
1W6S	3.15	$0.59_{(2)}$	$0.22_{(2)}$	$0.00_{(3)}$	$1.04_{(2)}$	$0.50_{(3)}$		
3H ₂ /1W6S		$1.74_{(2)}$	$1.80_{(2)}$					
2W6S	2.10	$0.10_{(4)}$	$0.03_{(1)}$	$0.00_{(1)}$	$0.13_{(3)}$	$0.52_{(3)}$	$0.82_{(2)}$	$0.61_{(4)}$
3H ₂ /2W6S		$1.96_{(3)}$	1.59(3)					
3W6S	5.25	$0.01_{(2)}$	$0.00_{(1)}$	$0.00_{(1)}$	$0.00_{(1)}$	$0.00_{(1)}$	$0.14_{(2)}$	$0.00_{(1)}$
3H ₂ /3W6S		$0.38_{(2)}$	0.47(2)					
MoS_2^{52}	6.00	0.31	0.36					
graphitic carbon nitride ⁶⁸	4.76	0.35	0.75		2.35			4.22
2D covalent triazine framework ⁶⁹	3.92	0.37	0.57		2.10		1.52	2.89
porous graphene ⁷⁰	3.75	0.35		0.60	2.00			2.60
porous graphene ⁷⁰	3.92	0.31		0.49	1.75			2.27
porous graphene ⁷⁰	5.50	0.10		0.18	0.62			1.56
Fused pentagon network ⁷¹	3.00			0.18	0.70		0.60	2.05
graphenylene ⁷²	5.34	0.03				0.84	0.57	2.02
graphenelike poly(triazine imide) ⁷³	3.88				0.12		0.26	
g-C ₂ O ⁷⁶	5.43	0.04			0.41		0.20	1.71

[&]quot;The subscript numbers in the parentheses refer to the type of interaction energy profile. For comparison, the barrier for translocation of the considered gases through other membranes is given.

On the other hand, only a 0.13 Å H-H bond extension was found for the absorption on the 2W6S or 3W6S pores. Depending on the orientation of the molecule and the number of W atoms at the edge, the H $_2$ adsorption energies, $E_{\rm ads}$, are found to be between -0.15 and -2.95 eV. These large adsorption energies are an indication of the high reactivity of W atoms at the pore. To analyze further, we performed abinitio MD simulations to verify the observed bond breaking in H $_2$. The details of the MD simulations are presented in the Methods section. It was found that the H-H bond length increases when H $_2$ approaches the 1W6S pore, and eventually the molecule is dissociated by attaching to W atoms as shown in Figure S3.

The observed dissociation of a single H₂ molecule and the corresponding bond length extension indicate that porous WS₂ may strongly interact with H₂ molecules. To probe this, we studied the hydrogenation of W dangling bonds present at the pore edge using additional H2 molecules. For simplicity, we considered the absorption of a maximum of three H₂ molecules; see Figure S4. We found that after H2 molecule adsorption, most of the W-H bonds become stretched, i.e., ≥1.85 Å, which are longer than the normal W-H bond (1.79 Å³¹). The latter is due to the charge transfer (of about 0.23lel) from the WS₂ monolayer to any adsorbed H atom (see Table 2). Our findings are consistent with the previous experimental results where a superior catalytic activity of transition metal dichalcogenide nanoporous films toward HER was reported.³² This type of catalytic activity has not been observed yet for porous WS2. However, our results indicate that the porous WS2 monolayer may have potential application as a catalyst for HER. Moreover, most of the adsorbed hydrogen atoms preferred to be oriented perpendicular to the WS₂ basal plane, instead of being in the pore plane (W atom plane). Therefore, the hydrogenation leads to partial blocking of translocation through the nanopore. The latter is consistent with a decrease in the pore area after hydrogen adsorption observed in the electron density isosurface (see the insets in Figures 1 and 2).

Translocation Energy Barrier. Next, we studied the important parameters that control both permeability and

selectivity and are related to the blocking of the nanopores. Using eq 1, we further calculated the translocation energy barrier (see Figure 3). The energy barriers (Δ) for the passage of He, H2, N2, CO2, and CH4 through the porous WS2 monolayers are listed in Table 3. We found that Δ is 2.91, 0.59, 0.10, and 0.01 eV for translocation of He through 1W, 1W6S, 2W6S, and 3W6S pores, respectively. For the 1W defect, the energy barrier for N2 was found to be the largest. Also, in most of the cases, the order of energy barriers is as follows: $H_2(\parallel) < H_2(\perp) < He < N_2(\parallel) < N_2(\perp)$. Because of larger k_{d} CO_2 and CH_4 gases do not translocate through the 1W and 1W6S pores. In the case of a 2W6S pore, the order of energy barrier follows $H_2(\parallel) < H_2(\perp) < He < N_2(\perp) < N_2$ (||) < CH₄ < CO₂. Hence, obviously, there is a relation between the pore size and k_d of gas molecules, where the Δ of a given gas molecule decreases for permeation through 1W, 1W6S, 2W6S, and 3W6S pores.

However, the large size of the pore limits its efficiency toward gas permeation. 77,78 Among the considered 2D lattice defects, 3W6S pores possess almost zero Δ for gas permeation, which renders gases capable of passing easily through the 3W6S pore. In the case of 1W6S and 2W6S pores, the difference between the Δ of H_2 (0.00–0.22 eV) and other gases is large, indicating that these types of defects can efficiently separate H_2 over He and N_2 .

In fact, due to the interaction between gases and the edge atoms of the nanopore, the kinetic diameter $(k_{\rm d})$ classical picture) is not the only criterion defining the translocation. In other words, a large overlap between the electron density (quantum picture) of gas molecules and porous WS₂ monolayers leads to a strong repulsive interaction. Consequently, the energy barrier of gas molecules increases with increasing overlap. The distinct Δ of $H_2(\parallel)$ for all pores compared to the other gases indicates the high selectivity of H_2 over other gases.

The analysis of the electron density in the pore center can provide a better understanding of the translocation energy barriers. Hence, the electron density isosurfaces of the He, H_2 , and N_2 gases passing through the porous WS_2 monolayers in the transition state (TS) structure, the state corresponding to

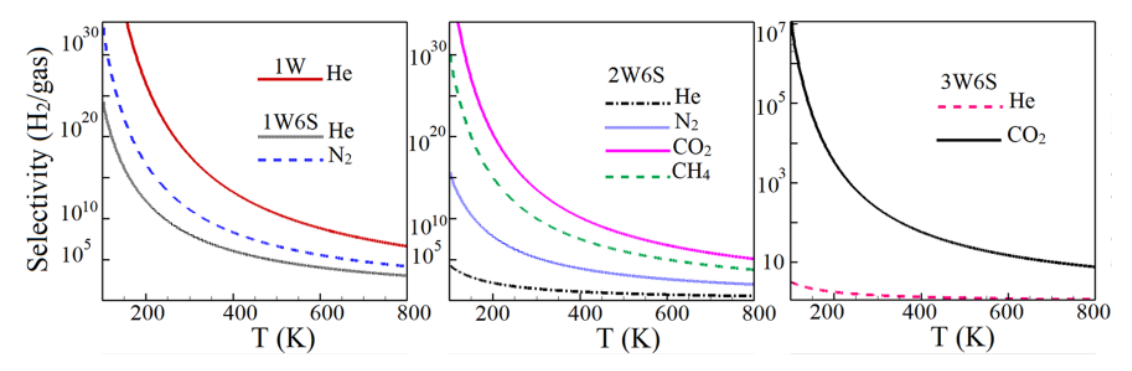


Figure 4. Selectivities (S) of the porous WS₂ monolayer for a gas mixture containing H_2 and different gases (He, N_2 CO₂ and CH₄) as a function of temperature.

the highest potential energy between two equilibrium states along the reaction pathway, are presented in Figure S5. The overlaps of the studied gases and the porous WS₂ monolayer follow the same sequence as $N_2 > H_2 > He$, which is attributed to the value order of k_d of each gas, i.e., 3.64 Å (N_2), 2.89 Å (H_2), and 2.60 Å (H_2).

Next, we investigated the influence of the pore edge saturation by H atoms on the translocation energy barrier of H_2 molecules. As expected, after edge saturation by H atoms, the translocation energy barrier increased due to the decrease of pore size. The results are presented in Figure 2. Also, the electron density isosurfaces of H_2 passing through the hydrogenated WS_2 monolayers in transition state (TS) structures are presented in Figure S6. Clearly, the overlap between electron densities in the perpendicular approach of H_2 is larger than that of the parallel approach.

To gain more insights, the important factors that control the energy barrier (Δ) can be qualitatively assessed from the classical formula, i.e., $\Delta_{\rm c} \simeq \frac{4\pi\epsilon D_{\rm p}}{L} \left(\frac{\sigma}{D_{\rm p}/2}\right)^{12}$, where ϵ and σ are

the Lennard-Jones potential parameters and L is the distance between the adjacent atoms on the pore edge. The fraction $\frac{\pi D_p}{L}$ gives the average number of atoms on the pore edge. This equation explicitly shows the dependence of the barrier on the size of the pore (via D_p), the strength of the interaction between particle and pore (via ϵ), and the number of atoms at the pore edge. While this formula provides useful qualitative insights, it quantitatively overestimates Δ . In contrast, the energy barriers obtained using DFT calculations are significantly smaller than those given by Δ_c . For example, for the 1W6S pore, Δ for translocation of the H_2 molecule by DFT is 0.59 eV, 2 orders of magnitude smaller than Δ_c .

Interaction Energy Profiles. The interaction energy between the atom/molecule and the porous membrane is discussed in this section. Figure 3 illustrates the interaction energy profiles of the gas molecules passing through 1W, 1W6S, 2W6S, and 3W6S pores. These pores are initially relaxed, but they are considered to be rigid during the translocation of particles. We cannot simultaneously relax the pore and calculate the translocation energy because the gas atom/molecule prefers to be adsorbed in the minimum-energy configuration. There are four types of profiles for these systems corresponding to the particles moving from one side to the other side through the center of the pores: (1) the interaction energy profiles without barrier, (2) profiles with a single barrier, (3) profiles with two barriers, and (4) profiles with

three barriers. In the transition-state (TS) configuration, the gas molecule is located almost near the center of the porous WS₂ pore, in the plane of W atoms (for type 2). In the TS configuration of type 3 profiles, the gas molecule is located near the S plane, and for type 4, the gas molecule is located close to both S and W planes. Notice that there is an essential difference between the interaction energy of particles with the strictly one-atom-thick membranes^{5,7,2,6,48} (such as graphene and hexagonal boron nitride) and TMDs (containing three sandwiched layers of atoms), where one-atom-thick membranes have only the aforementioned type 1 or 2 interaction energy profile. The types of interaction for each interaction energy profile are listed in Table 3.

Selectivity. By calculating Δ , one can determine the selectivity and permeance. The selectivity of a porous membrane is conventionally defined as

$$S_{X/Y} = \left(\frac{A_X e^{-\Delta_X/k_B T}}{A_Y e^{-\Delta_Y/k_B T}}\right) \tag{5}$$

where $\Delta_{X,Y}$ and T are the energy barrier (at zero temperature) and the temperature, respectively. We assume $A_X \simeq A_Y$ because the temperature of both gases is equal and the molar masses of the gases are of the same order of magnitude.

It is important to mention that the energy barrier can be slightly different with varying temperatures. The energy barrier against translocation of gas molecules can be different from the value at zero temperature due to different entropic contributions at the initial and saddle-point configurations and also due to the changes in the atomic geometry. The former contribution is normally quite small unless the temperature is high (well above the room temperature). As for the latter, the pores observed in the experiment $^{24,49-51}$ are mechanically stable with constant geometry. These observations led us to neglect the thermal fluctuation effects. Therefore, all of the energy barriers of the translocated molecules were calculated at zero temperature. We also note that independent of taking into account the temperature effects, our approach enabled us to determine which of the pores have the highest selectivity for a given gas molecule.

According to the collision theory, the frequency factor A depends on how often molecules collide and their orientation when they collide, and it is a temperature dependence parameter. The selectivity is usually measured at the same temperature for both gases. The latter implies $A_X = A_Y$. Also, binding molecules to the sheet may change the factor A. For each gas, the steric factor (ρ) instead of the frequency factor can be used $(\rho = A_{(after-adsorption)})/A_{(before-adsorption)}$, $0 < \rho < 1$).

Table 4. Selectivities (S) of the Porous WS₂ Monolayer for He, H₂, N₂, CO₂, and CH₄ Gas Mixtures at 300 K^a

membrane	H ₂ /He	H_2/N_2	H ₂ /CO ₂	H_2/CH_4
1W	4.4×10^{17}	7.1×10^{71}		
1W6S	1.2×10^{8}	1.2×10^{11}		
2W6S	26	1.6×10^{5}	3.4×10^{13}	9.9×10^{9}
3W6S	1.5	1	2.2×10^{2}	1
MoS_2^{25} (membrane thickness = 500 Å)			7.18	
MoS_2^{29} (6.00 Å)			1.40×10^{8}	
graphitic carbon nitride ⁶⁸ (4.76 Å)	1.0×10^{-7}			
CTF-0 ⁶⁹ (3.26 Å)		4.00×10^{24}	9.00×10^{13}	2.00×10^{36}
porous graphene ⁷⁰ (3.75-5.50 Å)			3.00×10^{23}	
Fused pentagon network ⁷¹ (3.00 Å)		1.00×10^{8}	1.00×10^{7}	1.00×10^{31}
polyphenylene ⁷⁹ (3.75 Å)	1.00×10^{1}	2.00×10^{23}	7.00×10^{16}	
polyphenylene ⁷⁹ (3.50 Å)		2.00×10^{23}	7.00×10^{16}	
γ-GYH ⁸⁰ (2.34 Å)		1.00×10^{26}	9.00×10^{17}	2.00×10^{49}
γ -GYN ⁸⁰ (2.42 Å)		2.00×10^{21}	2.00×10^{13}	2.00×10^{46}
phosphorene ⁸¹ (6.32 Å)		1.00×10^{13}	1.00×10^{15}	1.00×10^{21}
graphenylene ⁸² (3.20 Å)		1.00×10^{13}	1.00×10^{14}	1.00×10^{34}
germanene ⁸³ (4.93 Å)		1.00×10^{14}	1.00×10^{10}	1.00×10^{36}
graphene with line defect ²⁰ (3.60 Å)	7.0×10^{6}	2.00×10^{12}	1.00×10^{10}	4.00×10^{23}
GO/MoS ₂ ⁸⁴ (membrane thickness = 600 Å)			26.70	
GO/MoS ₂ ⁸⁴ (membrane thickness = 1500 Å)			44.20	
MoS_2^{85} (membrane thickness = 170 Å)			3.4	
MoS_2^{85} (membrane thickness = 350 Å)			3.7	
MoS_2^{85} (membrane thickness = 600 Å)			4.4	
comparison purposes, we listed selectivities of	other membranes.			

(a) (b) (c) H_2 Permeance (GPU) 10 10⁻¹ 10^{-6} 2W6S He He 10^{-6} H_2 H_2 H_2 He W CO_2 10^{-1} CH_4 10-16 10 600 800 800 200 400 200 400 600 200 600 800 T(K)T(K)T (K)

Figure 5. Permeance (P) of He, H_2 N_2 CO_2 and CH_4 penetrating through four porous WS_2 monolayers as a function of temperature: (a) 1W and 1W6S, (b) 2W6S, and (c) 3W6S. The acceptable industrial standard for gas separation is about 0.31×10^2 GPU in all temperatures. The density of the pores is considered to be $1/A_0$, where $A_0 \simeq 5$ nm².

This assumption may be made since the selectivity is very large, i.e., $O(10^n)$ where n > 5.

Note that the highest selectivity is for molecules that have a size comparable to the pore size. The selectivity of the gases penetrating the 1W, 1W6S, 2W6S, and 3W6S pores as a function of temperature is shown in Figure 4. At a given temperature, the selectivity increases with the mass of the translocating molecule. For a gas mixture (X/Y) over 1W6S pore, the selectivity follows the order $H_2/N_2 > H_2/He$. For the case of the 2W6S pore, the selectivity order is $H_2/CO_2 > H_2/CH_4 > H_2/N_2 > H_2/He$. For a gas mixture of H_2 and N_2 , the selectivity on the 1W6S pore is higher than that of the 2W6S pore, even when the temperature reaches 600 K. The selectivities of the studied gases at 300 K are tabulated in Table 4.

Both the interaction energy profile and selectivity results confirm that the WS_2 monolayers with the 1W6S pores have a

high potential for gas separation ($S \simeq 10^9$). In contrast, the monolayer with the 3W6S pores is not selective for He, H₂, and N₂ gases, due to the pore size limit. For the mixture of H₂ and CO₂, the selectivities of 3W6S pores are on the order of $\simeq 10^2$ at room temperature. For comparison, in Table 4, the selectivities of our studied porous WS₂ monolayers are compared with those of other membranes for various gases.

Permeance. Next, to evaluate the separation efficiency of the porous WS₂ monolayers, the permeance (P) of the molecules is calculated. The cross-sectional area A of the pores is estimated according to ref 24 (see Table S1). The details of the permeance calculations are presented in the Methods section. The calculated ratios of the cross-sectional area ($\alpha = A/A_0$) values are 0.002, 0.016, 0.026, and 0.044 for 1W, 1W6S, 2W6S, and 3W6S pores, respectively. The density of the pores is considered to be $1/A_0$, where $A_0 \simeq 5$ nm² (this is a high density of pores). Obviously, for the smaller density of pores,

Table 5. Permeance (P, GPU) of the Porous WS₂ Monolayer for He, H₂, N₂, CO₂, and CH₄ Gases at 300 K^a

membrane	He	H_2	N_2	CO_2	CH_4		
1W	0.00	0.00	0.00				
1W6S	0.74×10^{-2}	17.54×10^4	0.27×10^{-6}				
2W6S	20.92×10^4	11.38×10^{6}	12.92	0.05×10^{-6}	0.28×10^{-3}		
3W6S	11.69×10^6	33.85×10^6	6.48×10^6	22.77×10^3	8.61×10^{6}		
fused pentagon network ⁷¹ (3.00 Å)		3.10×10^{7}					
GO/MoS_2^{84} (membrane thickness = 600 Å)		2.47×10^{2}	10.61×10^{2}				
GO/MoS_2^{84} (membrane thickness = 1500 Å)		8.83×10^{2}					
MoS_2^{85} (membrane thickness = 170 Å)	2.45×10^4	2.74×10^4	9.19×10^{3}	8.13×10^{3}	1.15×10^{4}		
MoS_2^{85} (membrane thickness = 350 Å)	5.22×10^{3}	7.04×10^{3}	2.30×10^{3}	1.91×10^{3}	3.06×10^{3}		
MoS_2^{85} (membrane thickness = 600 Å)	1.77×10^{3}	2.44×10^{3}	7.80×10^{2}	5.60×10^{2}	8.84×10^{2}		
The density of the pores is considered to be $1/A_0$, where $A_0 \simeq 5 \text{ nm}^2$ (this is a high density of pores).							

the permeance is smaller. Figure 5 displays the permeance (P) of He, H₂, N₂, CO₂, and CH₄ through four porous WS₂ monolayers. It is clear that P increases significantly with increasing temperature, while the efficiency for filtration, i.e., the difference between the permeance of the studied gases, decreases at larger temperatures. The permeance is inversely proportional to $k_{\rm d}$. It is important to mention that by neglecting the reflected atom/molecules from the pore edge, the calculated P in this study might be the upper limit of what can be observed experimentally.

In the case of He, H_2 , and N_2 penetrating through 2W6S pores, at about 380 K (see Figure 5), the permeance can exceed the industrial production limit (0.31 \times 10² GPU; 1 GPU = 3.25×10^{-10} mol m⁻² s⁻¹ Pa⁻¹).⁷⁶ As a result, the 2W6S pores are interesting candidates to permeate He, H2, and N2 gases for practical applications. The permeance of the studied gases at 300 K is tabulated in Table 5. Moreover, the P of $H_2(\perp)$ and $H_2(\perp)$ reaches the industrial production limit at about 200 and 450 K, respectively. Figure 5 shows that the 3W6S nanopore has a relatively high permeance of the studied gases in the order of $H_2 > He > CH_4 > N_2 > CO_2$ at 100-800K in a range of 10^3-10^6 GPU. The permeances of our studied porous WS₂ monolayers are compared to those of other membranes in Table 5. The permeance of the MoS₂ membrane (with thicknesses of 170, 350, and 600 Å) for gas separation is compared with our results for the WS₂ monolayer (see Table 5). It is found that the permeance of H₂ through porous WS₂ monolayers is higher than that of MoS₂ membranes. Also, the permeance of H2, He, CH4, N2, and CO2 gases through the 3W6S pore is higher than that of the MoS₂ membrane.

CONCLUSIONS

Gas transport through WS₂ monolayers with four types of pores was explored using the first-principles calculations. The pore sizes, defined as 1W, 1W6S, 2W6S, and 3W6S, were 1.05, 3.15, 2.10, and 5.25 Å, respectively. Accordingly, the monolayer with 1W6S pores was found to be permeable and able to separate gases in a mixture of H_2/He and H_2/N_2 . The energy barrier for the translocation of a gas molecule through a porous WS₂ monolayer was found to be dependent on the kinetic diameter and the direction in which the gas molecule approaches the pore (perpendicular, \(\perp\), or parallel, \(\| \)). The interaction energy profiles show that H2 (in || direction) has the lowest barrier when passing through the porous WS2 monolayer. A remarkable result is that the $H_2(||)$ dissociates when it is located in the W plane of the 1W6S pore. This causes a pore edge saturation by H atoms. Moreover, electron density isosurface calculations demonstrate that N2 has more

pronounced electron overlaps than He and H₂ in porous WS₂ monolayers, which is due to the stronger repulsive interaction between porous monolayers and N₂. Both experimental and ab-initio molecular dynamics results confirm the high mechanical stability of the studied porous WS₂. Based on these results, WS₂ monolayers may have a great potential for gas separation, possibly surpassing the characteristics of porous graphene membranes. Our findings suggest that defective WS₂ monolayers can be used as a potentially new hydrogen storage platform that warrants future experimental investigations to validate such applications.

ASSOCIATED CONTENT

5 Supporting Information

The Supporting Information is available free of charge at https://pubs.acs.org/doi/10.1021/acs.jpcc.1c06894.

Molecular electrostatic potential map of the studied porous WS_2 monolayer (Figure S1); optimized structure of 1W and 3W6S monolayers at room temperature (Figure S2); most favorable sites for the adsorption of various gases on the porous WS_2 monolayer (Figure S3); optimized structures of the hydrogenated porous WS_2 monolayers (Figure S4); electron density isosurfaces for TS structures of the studied gases on the porous WS_2 monolayer (Figures S5 and S6); simulation setup to inject a typical atom/molecule onto the porous WS_2 monolayer (Figure S7); optimized crystal lattice parameters, the cross-sectional area, and the supercell area of the studied porous WS_2 monolayers (Table S1); and isotropic polarizabilities of the studied gases (Table S2) (PDF)

AUTHOR INFORMATION

Corresponding Author

Mehdi Neek-Amal — Department of Physics, Shahid Rajaee Teacher Training University, Tehran 16875-163, Iran; Departement Fysica, Universiteit Antwerpen, Antwerpen B-2020, Belgium; orcid.org/0000-0001-7277-6965; Email: mehdi.neek-amal@uantwerpen.be

Authors

Nasim Hassani — Department of Physics, Shahid Rajaee Teacher Training University, Tehran 16875-163, Iran; orcid.org/0000-0002-5386-1280

Mahdi Ghorbani-Asl — Institute of Ion Beam Physics and Materials Research, Helmholtz-Zentrum Dresden-Rossendorf, 01328 Dresden, Germany; orcid.org/0000-0003-3060-4369

- Boya Radha Department of Physics & Astronomy, School of Natural Sciences, University of Manchester, Manchester M13 9PL, U.K.
- Marija Drndić Department of Physics and Astronomy, University of Pennsylvania, Philadelphia, Pennsylvania 19104, United States
- Arkady V. Krasheninnikov Institute of Ion Beam Physics and Materials Research, Helmholtz-Zentrum Dresden-Rossendorf, 01328 Dresden, Germany; Department of Applied Physics, Aalto University, 00076 Aalto, Finland; orcid.org/0000-0003-0074-7588

Complete contact information is available at: https://pubs.acs.org/10.1021/acs.jpcc.1c06894

Notes

The authors declare no competing financial interest.

ACKNOWLEDGMENTS

A.V.K. acknowledges funding from DFG through project KR 4866/2-1 (406129719). The authors thank HRLS Stuttgart, Germany, and TU Dresden (Taurus cluster) for the generous grant of computer time. The authors appreciate the computational resources and software provided by Shahid Rajaee Teacher Training University. B.R. acknowledges the Royal Society University Research Fellowship and Enhancement Award RGF EA 181000 and ERC Starting Grant Agreement Number 852674—AngstroCAP. N.H. and M.N.-A. gratefully acknowledge the support of the Iran National Science Foundation (INSF). M.D. acknowledges support from NSF DMR 1905045 and NSF CCMI Advanced Manufacturing (AM) grant 2002477.

REFERENCES

- (1) Kirby, B. J. Micro-and Nanoscale Fluid Mechanics: Transport in Microfluidic Devices; Cambridge University Press, 2010; pp 60-61.
- (2) Wang, L.; Boutilier, M. S.; Kidambi, P. R.; Jang, D.; Hadjiconstantinou, N. G.; Karnik, R. Fundamental transport mechanisms, fabrication and potential applications of nanoporous atomically thin membranes. *Nat. Nanotechnol.* **2017**, *12*, 509.
- (3) Kozubek, R.; Tripathi, M.; Ghorbani-Asl, M.; Kretschmer, S.; Madauß, L.; Pollmann, E.; O'Brien, M.; McEvoy, N.; Ludacka, U.; Susi, T.; et al. Perforating freestanding molybdenum disulfide monolayers with highly charged ions. *J. Phys. Chem. Lett.* **2019**, *10*, 904–910.
- (4) Lehnert, T.; Ghorbani-Asl, M.; Köster, J.; Lee, Z.; Krasheninnikov, A. V.; Kaiser, U. Electron-beam-driven structure evolution of single-layer MoTe₂ for quantum devices. *ACS Appl. Nano Mater.* **2019**, *2*, 3262–3270.
- (5) Koenig, S. P.; Wang, L.; Pellegrino, J.; Bunch, J. S. Selective molecular sieving through porous graphene. *Nat. Nanotechnol.* **2012**, 7, 728-732.
- (6) Yuan, Q.; Yin, A. X.; Luo, C.; Sun, L. D.; Zhang, Y. W.; Duan, W. T.; Liu, H. C.; Yan, C. H. Facile synthesis for ordered mesoporous γ-aluminas with high thermal stability. J. Am. Chem. Soc. 2008, 130, 3465–3472.
- (7) Yuan, Z.; Govind Rajan, A.; Misra, R. P.; Drahushuk, L. W.; Agrawal, K. V.; Strano, M. S.; Blankschtein, D. Mechanism and prediction of gas permeation through sub-nanometer graphene pores: comparison of theory and simulation. ACS Nano 2017, 11, 7974–7987.
- (8) Yuan, Z.; Misra, R. P.; Rajan, A. G.; Strano, M. S.; Blankschtein, D. Analytical Prediction of Gas Permeation through Graphene Nanopores of Varying Sizes: Understanding Transitions across Multiple Transport Regimes. ACS Nano 2019, 13, 11809–11824.

- (9) Yuan, Z.; Benck, J. D.; Eatmon, Y.; Blankschtein, D.; Strano, M. S. Stable, temperature-dependent gas mixture permeation and separation through suspended nanoporous single-layer graphene membranes. *Nano Lett.* **2018**, *18*, 5057–5069.
- (10) Thiruraman, J. P.; Masih Das, P.; Drndić, M. Irradiation of Transition Metal Dichalcogenides Using a Focused Ion Beam: Controlled Single-Atom Defect Creation. *Adv. Funct. Mater.* **2019**, 29, No. 1904668.
- (11) Boutilier, M. S.; Jang, D.; Idrobo, J. C.; Kidambi, P. R.; Hadjiconstantinou, N. G.; Karnik, R. Molecular sieving across centimeter-scale single-layer nanoporous graphene membranes. ACS Nano 2017, 11, 5726–5736.
- (12) Surwade, S. P.; Smirnov, S. N.; Vlassiouk, I. V.; Unocic, R. R.; Veith, G. M.; Dai, S.; Mahurin, S. M. Water desalination using nanoporous single-layer graphene. *Nat. Nanotechnol.* **2015**, *10*, 459–464.
- (13) Zhao, F.; Peydayesh, M.; Ying, Y.; Mezzenga, R.; Ping, J. Transition Metal Dichalcogenide—Silk Nanofibril Membrane for One-Step Water Purification and Precious Metal Recovery. ACS Appl. Mater. Interfaces 2020, 12, 24521—24530.
- (14) Schrier, J. Carbon dioxide separation with a two-dimensional polymer membrane. ACS Appl. Mater. Interfaces 2012, 4, 3745–3752.
- (15) Schrier, J. Fluorinated and nanoporous graphene materials as sorbents for gas separations. ACS Appl. Mater. Interfaces 2011, 3, 4451–4458.
- (16) Shan, M.; Xue, Q.; Jing, N.; Ling, C.; Zhang, T.; Yan, Z.; Zheng, J. Influence of chemical functionalization on the CO_2/N_2 separation performance of porous graphene membranes. *Nanoscale* **2012**, *4*, 5477–5482.
- (17) Du, H.; Li, J.; Zhang, J.; Su, G.; Li, X.; Zhao, Y. Separation of hydrogen and nitrogen gases with porous graphene membrane. *J. Phys. Chem. C* **2011**, *115*, 23261–23266.
- (18) Wen, B.; Sun, C.; Bai, B. Inhibition effect of a non-permeating component on gas permeability of nanoporous graphene membranes. *Phys. Chem. Phys.* **2015**, *17*, 23619–23626.
- (19) Sun, C.; Boutilier, M. S.; Au, H.; Poesio, P.; Bai, B.; Karnik, R.; Hadjiconstantinou, N. G. Mechanisms of molecular permeation through nanoporous graphene membranes. *Langmuir* **2014**, *30*, 675–682
- (20) Qin, X.; Meng, Q.; Feng, Y.; Gao, Y. Graphene with line defect as a membrane for gas separation: Design via a first-principles modeling. Surf. Sci. 2013, 607, 153–158.
- (21) Liu, H.; Chen, Z.; Dai, S.; Jiang, D. E. Selectivity trend of gas separation through nanoporous graphene. *J. Solid State Chem.* **2015**, 224. 2–6.
- (22) Sun, P. Z.; Yagmurcukardes, M.; Zhang, R.; Kuang, W. J.; Lozada-Hidalgo, M.; Wang, F. C.; Peeters, F. M.; Grigorieva, I. V.; Geim, A. K. Exponentially selective molecular sieving through angstrom pores, 2021. arXiv:2104.02560. https://arxiv.org/abs/2104.02560.
- (23) Griffin, E.; Mogg, L.; Hao, G. P.; Kalon, G.; Bacaksiz, C.; Lopez-Polin, G.; Zhou, T. Y.; Guarochico, V.; Cai, J.; Neumann, C.; Winter, A.; et al. Proton and Li-ion permeation through graphene with eight-atom-ring defects. ACS Nano 2020, 14, 7280–7286.
- (24) Thiruraman, J. P.; Dar, S. A.; Das, P. M.; Hassani, N.; Neek-Amal, M.; Keerthi, A.; Drndić, M.; Radha, B. Gas flow through atomic-scale apertures. *Sci. Adv.* 2020, 6, No. eabc7927.
- (25) Achari, A.; Sahana, S.; Eswaramoorthy, M. High performance MoS₂ membranes: effects of thermally driven phase transition on CO₂ separation efficiency. *Energy Environ. Sci.* **2016**, *9*, 1224–1228.
- (26) Zhang, Y.; Shi, Q.; Liu, Y.; Wang, Y.; Meng, Z.; Xiao, C.; Deng, K.; Rao, D.; Lu, R. Hexagonal boron nitride with designed nanopores as a high-efficiency membrane for separating gaseous hydrogen from methane. J. Phys. Chem. C 2015, 119, 19826—19831.
- (27) Zhang, Y.; Meng, Z.; Shi, Q.; Gao, H.; Liu, Y.; Wang, Y.; Rao, D.; Deng, K.; Lu, R. Nanoporous MoS₂ monolayer as a promising membrane for purifying hydrogen and enriching methane. *J. Phys.: Condens. Matter* **2017**, *29*, No. 375201.

- (28) Ghorbani-Asl, M.; Kretschmer, S.; Spearot, D. E.; Krasheninnikov, A. V. Two-dimensional MoS₂ under ion irradiation: from controlled defect production to electronic structure engineering. 2D Mater. 2017, 4, No. 025078.
- (29) Yin, K.; Huang, S.; Chen, X.; Wang, X.; Kong, J.; Chen, Y.; Xue, J. Generating sub-nanometer pores in single-layer MoS₂ by heavy-ion bombardment for gas separation: a theoretical perspective. ACS Appl. Mater. Interfaces 2018, 10, 28909–28917.
- (30) Jaramillo, T. F.; Jorgensen, K. P.; Bonde, J.; Nielsen, J. H.; Horch, S.; Chorkendorff, I. Identification of active edge sites for electrochemical H₂ evolution from MoS₂ nanocatalysts. *Science* **2007**, 317, 100–102.
- (31) Tanjaroon, C.; Keck, K. S.; Sebonia, M. M.; Karunatilaka, C.; Kukolich, S. G. Microwave spectra and the metal-hydrogen bond lengths for the $C_5H_5Mo(CO)_3H$ and $C_5H_5W(CO)_3H$ complexes. *J. Chem. Phys.* **2004**, *121*, 1449–1453.
- (32) Yang, Y.; Fei, H.; Ruan, G.; Xiang, C.; Tour, J. M. Edgeoriented MoS₂ nanoporous films as flexible electrodes for hydrogen evolution reactions and supercapacitor devices. *Adv. Mater.* **2014**, *26*, 8163–8168
- (33) Mohanty, B.; Ghorbani-Asl, M.; Kretschmer, S.; Ghosh, A.; Guha, P.; Panda, S. K.; Jena, B.; Krasheninnikov, A. V.; Jena, B. K. MoS₂ quantum dots as efficient catalyst materials for the oxygen evolution reaction. *ACS Catal.* **2018**, *8*, 1683–1689.
- (34) Han, S. W.; Cha, G. B.; Park, Y.; Hong, S. C. Hydrogen physisorption based on the dissociative hydrogen chemisorption at the sulphur vacancy of MoS₂ surface. *Sci. Rep.* **2017**, *7*, No. 7152.
- (35) Dai, W. J.; Gan, Y. X.; Hanaor, D. Effective thermal conductivity of submicron powders: a numerical study. *Appl. Mech. Mater.* **2016**, 846, 500–505.
- (36) Luty, B. A.; van Gunsteren, W. F. Calculating electrostatic interactions using the particle-particle particle-mesh method with nonperiodic long-range interactions. *J. Phys. Chem. A.* **1996**, *100*, 2581–2587.
- (37) Pechukas, P. Transition state theory. Annu. Rev. Phys. Chem. 1981, 32, 159-177.
- (38) Liu, H.; Dai, S.; Jiang, D. E. Insights into CO₂/N₂ separation through nanoporous graphene from molecular dynamics. *Nanoscale* **2013**, *5*, 9984–9987.
- (39) Vahdat, M. T.; Campi, D.; Colonna, N.; Villalobos, L. F.; Marzari, N.; Agrawal, K. V. Efficient Kr/Xe separation from triangular gC₃N₄ nanopores, a simulation study. *J. Mater. Chem. A* **2020**, 8, 17747–17755.
- (40) Sun, C.; Wen, B.; Bai, B. Application of nanoporous graphene membranes in natural gas processing: Molecular simulations of CH₄/CO₂, CH₄/H₂S and CH₄/N₂ separation. *Chem. Eng. Sci.* **2015**, *138*, 616–621.
- (41) Yuan, Z.; Govind Rajan, A.; He, G.; Misra, R. P.; Strano, M. S.; Blankschtein, D. Predicting Gas Separation through Graphene Nanopore Ensembles with Realistic Pore Size Distributions. ACS Nano 2021, 15, 1727–1740.
- (42) Cranford, S. W.; Buehler, M. J. Selective hydrogen purification through graphdiyne under ambient temperature and pressure. *Nanoscale* **2012**, *4*, 4587–4593.
- (43) Huang, C.; Wu, H.; Deng, K.; Tang, W.; Kan, E. Improved permeability and selectivity in porous graphene for hydrogen purification. *Phys. Chem. Chem. Phys.* **2014**, *16*, 25755–25759.
- (44) Schrier, J. Helium separation using porous graphene membranes. J. Phys. Chem. Lett. 2010, 1, 2284–2287.
- (45) Tao, Y.; Xue, Q.; Liu, Z.; Shan, M.; Ling, C.; Wu, T.; Li, X. Tunable hydrogen separation in porous graphene membrane: first-principle and molecular dynamic simulation. ACS Appl. Mater. Interfaces 2014, 6, 8048–8058.
- (46) Jiang, D. E.; Cooper, V. R.; Dai, S. Porous graphene as the ultimate membrane for gas separation. *Nano Lett.* **2009**, *9*, 4019–4024
- (47) Wang, S.; Dai, S.; Jiang, D. E. Continuously tunable pore size for gas separation via a bilayer nanoporous graphene membrane. ACS Appl. Nano Mater. 2019, 2, 379–384.

- (48) Lin, S.; Xu, M.; Qu, Z.; Liang, Y.; Li, Y.; Cui, W.; Shi, J.; Zeng, Q.; Hao, J.; Li, Y. Hidden porous boron nitride as a high-efficiency membrane for hydrogen purification. *Phys. Chem. Chem. Phys.* **2020**, 22, 22778–22784.
- (49) Thiruraman, J. P.; Masih Das, P.; Drndić, M. Stochastic Ionic Transport in Single Atomic Zero-Dimensional Pores. *ACS Nano* **2020**, *14*, 11831–11845.
- (50) Zheng, X.; Calò, A.; Cao, T.; Liu, X.; Huang, Z.; Das, P. M.; Drndic, M.; Albisetti, E.; Lavini, F.; Narang, V.; et al. Spatial defects nanoengineering for bipolar conductivity in MoS₂. *Nat. Commun.* **2020**, *11*, No. 3463.
- (51) Masih Das, P.; Drndić, M. In Situ 2D MoS₂ Field-Effect Transistors with an Electron Beam Gate. ACS Nano 2020, 14, 7389—7397
- (52) Azamat, J.; Khataee, A. MoS₂ nanosheet as a promising nanostructure membrane for gas separation. *J. Ind. Eng. Chem.* **2018**, 66, 269–278.
- (53) Sapkota, B.; Liang, W.; VahidMohammadi, A.; Karnik, R.; Noy, A.; Wanunu, M. High permeability sub-nanometre sieve composite MoS₂ membranes. *Nat. Commun.* **2020**, *11*, No. 2747.
- (54) Delley, B. From molecules to solids with the DMol³ approach. *J. Chem. Phys.* **2000**, *113*, 7756–7764.
- (55) Perdew, J. P.; Burke, K.; Ernzerhof, M. Generalized gradient approximation made simple. *Phys. Rev. Lett.* **1996**, *77*, No. 3865.
- (56) Delley, B. An all-electron numerical method for solving the local density functional for polyatomic molecules. *J. Chem. Phys.* **1990**, 92, 508–517.
- (57) Govind, N.; Petersen, M.; Fitzgerald, G.; King-Smith, D.; Andzelm, J. A generalized synchronous transit method for transition state location. *Comput. Mater. Sci.* **2003**, 28, 250–258.
- (58) Tkatchenko, A.; Scheffler, M. Accurate molecular van der Waals interactions from ground-state electron density and free-atom reference data. *Phys. Rev. Lett.* **2009**, *102*, No. 073005.
- (59) Hirshfeld, F. L. Bonded-atom fragments for describing molecular charge densities. *Theor. Chim. Acta* 1977, 44, 129–138.
- (60) Kresse, G.; Furthmüller, J. Efficient iterative schemes for ab initio total-energy calculations using a plane-wave basis set. *Phys. Rev.* B 1996, 54, No. 11169.
- (61) Zhou, S.; Wang, Z.; Wang, M.; Wang, J.; Wei, S.; Guo, W.; Lu, X. Nanoporous boron nitride membranes for helium separation. ACS Appl. Nano Mater. 2019, 2, 4471–4479.
- (62) Ma, L.; Tan, Y.; Ghorbani-Asl, M.; Boettger, R.; Kretschmer, S.; Zhou, S.; Huang, Z.; Krasheninnikov, A. V.; Chen, F. Tailoring the optical properties of atomically-thin WS₂ via ion irradiation. *Nanoscale* **2017**, *9*, 11027–11034.
- (63) Kretschmer, S.; Maslov, M.; Ghaderzadeh, S.; Ghorbani-Asl, M.; Hlawacek, G.; Krasheninnikov, A. V. Supported two-dimensional materials under ion irradiation: The substrate governs defect production. ACS Appl. Mater. Interfaces 2018, 10, 30827–30836.
- (64) Chemical Applications of Atomic and Molecular Electrostatic Potentials: Reactivity, Structure, Scattering, and Energetics of Organic, Inorganic, and Biological Systems; In Politzer, P.; Truhlar, D. G., Eds.; Springer Science & Business Media, 2013.
- (65) Leiva, P.; Piris, M. natural orbital functional study for the electric response properties of molecules. *J. Theor. Comput. Chem.* **2005**, *04*, 1165–1173.
- (66) Lewis, M.; Wu, Z.; Glaser, R. Polarizabilities of carbon dioxide and carbodiimide. Assessment of theoretical model dependencies on dipole polarizabilities and dipole polarizability anisotropies. *J. Phys. Chem. A* 2000, 104, 11355–11361.
- (67) Pham, V. D.; Joucken, F.; Repain, V.; Chacon, C.; Bellec, A.; Girard, Y.; Rousset, S.; Sporken, R.; Dos Santos, M. C.; Lagoute, J. Molecular adsorbates as probes of the local properties of doped graphene. *Sci. Rep.* **2016**, *6*, No. 24796.
- (68) Li, F.; Qu, Y.; Zhao, M. Efficient helium separation of graphitic carbon nitride membrane. *Carbon* **2015**, *95*, 51–57.
- (69) Wang, Y.; Li, J.; Yang, Q.; Zhong, C. Two-dimensional covalent triazine framework membrane for helium separation and hydrogen purification. ACS Appl. Mater. Interfaces 2016, 8, 8694–8701.

- (70) Wei, S.; Zhou, S.; Wu, Z.; Wang, M.; Wang, Z.; Guo, W.; Lu, X. Mechanistic insights into porous graphene membranes for helium separation and hydrogen purification. *Appl. Surf. Sci.* **2018**, *441*, 631–638.
- (71) Zhu, L.; Xue, Q.; Li, X.; Jin, Y.; Zheng, H.; Wu, T.; Guo, Q. Theoretical prediction of hydrogen separation performance of two-dimensional carbon network of fused pentagon. ACS Appl. Mater. Interfaces 2015, 7, 28502–28507.
- (72) Wang, L.; Li, F.; Wang, J.; Li, Y.; Li, W.; Yang, Y.; Zhao, M.; Qu, Y. High-efficiency helium separation through an inorganic graphenylene membrane: a theoretical study. *Phys. Chem. Chem. Phys.* **2020**, 22, 9789–9795.
- (73) Wang, Y.; Yang, Q.; Zhong, C.; Li, J. Graphene-like poly (triazine imide) as N₂-selective ultrathin membrane for postcombustion CO₂ capture. *J. Phys. Chem. C* **2016**, *120*, 28782–28788.
- (74) Zhou, C.; Yang, W.; Zhu, H. Mechanism of charge transfer and its impacts on Fermilevel pinning for gas molecules adsorbed on monolayer WS₂. *J. Chem. Phys.* **2015**, *142*, No. 214704.
- (75) Zhou, J.; Cao, J.; Shi, J.; Zhang, Y.; Chen, J.; Wang, W.; Liu, X. A WS₂ Case Theoretical Study: Hydrogen Storage Performance Improved by Phase Altering. *Nanoscale Res. Lett.* **2020**, *15*, No. 102.
- (76) Liu, X.; Chang, X.; Zhu, L.; Li, X. High-efficiency helium separation through g-C₂O membrane: A theoretical study. *Comput. Mater. Sci.* **2019**, *157*, 1–5.
- (77) Peymanirad, F.; Neek-Amal, M.; Beheshtian, J.; Peeters, F. M. Graphene-silicene bilayer: A nanocapacitor with permanent dipole and piezoelectricity effect. *Phys. Rev. B* **2015**, 92, No. 155113.
- (78) Galashev, A. Y.; Katin, K. P.; Maslov, M. M. Morse parameters for the interaction of metals with graphene and silicene. *Phys. Lett. A* **2019**, 383, 252–258.
- (79) Blankenburg, S.; Bieri, M.; Fasel, R.; Müllen, K.; Pignedoli, C. A.; Passerone, D. Porous graphene as an atmospheric nanofilter. *Small* **2010**, *6*, 2266–2271.
- (80) Sang, P.; Zhao, L.; Xu, J.; Shi, Z.; Guo, S.; Yu, Y.; Zhu, H.; Yan, Z.; Guo, W. Excellent membranes for hydrogen purification: Dumbbell-shaped porous g-graphynes. *Int. J. Hydrogen Energy* **2017**, 42, 5168–5176.
- (81) Zhang, Y.; Hao, F.; Xiao, H.; Liu, C.; Shi, X.; Chen, X. Hydrogen separation by porous phosphorene: A periodical DFT study. *Int. J. Hydrogen Energy* **2016**, *41*, 23067–23074.
- (82) Song, Q.; Wang, B.; Deng, K.; Feng, X.; Wagner, M.; Gale, J. D.; Müllen, K.; Zhi, L. Graphenylene, a unique two-dimensional carbon network with nondelocalized cyclohexatriene units. *J. Mater. Chem. C* 2013, 1, 38–41.
- (83) Chang, X.; Xue, Q.; He, D.; Zhu, L.; Li, X.; Tao, B. 585 divacancy-defective germanene as a hydrogen separation membrane: A DFT study. *Int. J. Hydrogen Energy* **2017**, *42*, 24189–24196.
- (84) Ostwal, M.; Shinde, D. B.; Wang, X.; Gadwal, I.; Lai, Z. Graphene oxide-molybdenum disulfide hybrid membranes for hydrogen separation. *J. Membr. Sci.* **2018**, *550*, 145–154.
- (85) Wang, D.; Wang, Z.; Wang, L.; Hu, L.; Jin, J. Ultrathin membranes of single-layered MoS₂ nanosheets for high-permeance hydrogen separation. *Nanoscale* **2015**, *7*, 17649–17652.
- (86) Jiang, D. E.; Sumpter, B. G.; Dai, S. Unique chemical reactivity of a graphene nanoribbon's zigzag edge. *J. Chem. Phys.* **2007**, *126*, No. 134701.